Automatic Segmentation Framework of Building Anatomical Mouse Model for Bioluminescence Tomography

Abdullah Alali
School of Computer Science and Engineering, Beihang University, Beijing, China
e-mail: Abdullah.M.F.Alali@gmail.com

Abstract

Bioluminescence tomography is known as a highly ill-posed inverse problem. To improve the reconstruction performance by introducing anatomical structures as a priori knowledge, an automatic segmentation framework has been proposed in this paper to extract the mouse whole-body organs and tissues, which enables to build up a heterogeneous mouse model for reconstruction of bioluminescence tomography. Finally, an in vivo mouse experiment has been conducted to evaluate this framework by using an X-ray computed tomography system and a multi-view bioluminescence imaging system. The findings suggest that the proposed method can realize fast automatic segmentation of mouse anatomical structures, ultimately enhancing the reconstruction performance of bioluminescence tomography.

Keywords: medical image processing, image segmentation, anatomical mouse model

1. Introduction

Bioluminescence tomography is one of the optical molecular imaging modalities, enabling real-time non-invasive in vivo imaging of labelled molecules in biological organisms. Due to its high sensitivity and low cost, bioluminescence tomography has attracted much attention over the past decade [1-3]. It is capable of obtaining three-dimensional distribution of the internal bioluminescent signal source, providing an effective way of information acquisition and quantitative analysis for disease progression, tumour detection as well as drug efficacy [4-6]. One of the challenges of bioluminescence tomography is that multiple scattering of photons propagating through biological tissues makes reconstruction a highly ill-posed problem. As reported in related existing literature, researchers have proposed some methods to solve the inverse problem, including permissible source region approach, multi-spectral information based algorithm and so on [7-10]. The basic idea is to reduce the number of unknown variables or to increase the amount of known boundary measurements for reconstruction that is mathematically a set of undetermined linear equations.

Similarly, to attain more information as *a priori* knowledge for bioluminescence tomography, we utilized anatomical structures of the experimental mouse in this paper. The gold standard to extract the anatomical structures is using manual segmentation. It usually takes hours to complete the entire interactive procedure even by a skilled user. With the rapid development of automatic segmentation algorithms, the processing efficiency has been significantly improved [11-15]. However, most methods are developed for some specific organs or tissues, requiring interactive operations, which are not appropriate for whole-body automatic applications. Therefore, a general automatic segmentation framework has been proposed in this paper to extract the whole-body anatomical structures of the experimental mouse, which could be applied to build a heterogeneous mouse model to enhance the performance of bioluminescence tomography.

2. Research Method

To acquire the experimental datasets, the Caliper Life Science's Spectrum CT was used, which is an integrative platform that combines bioluminescence and fluorescence imaging with X-Ray CT scanning. Here, two modalities including bioluminescence imaging and X-Ray

CT were applied to the following experiment. For X-Ray imaging, the cone-beam X-ray generator was operated in a continuous mode with the tube voltage being 45kVp, where 360° projections were scanned. For bioluminescence imaging, a cooled CCD with 13.5µm×13.5µm pixel size was involved in taking the multi-views of the optical images. The experimental mouse was injected through the caudal tail vein with Fenestra LC which is an iodinated lipid emulsion bloodpool contrast agent helping overcome the problem of inherently soft tissue contrast in CT imaging, followed by 0.3ml of anesthetic at a 0.15g/ml concentration via intraperitoneal injection. Then, a home-made luminescent bead was implanted into the mouse. Since the luminescent bead was wrapped in a plastic material, it could be easily detected by CT, enabling examination of the reconstruction accuracy of bioluminescence imaging.

2.1. Automatic Segmentation Framework
2.1.1. Bone structures

To automatically extract bone structures, a thresholding method based on the principle of maximum entropy was utilized here, because the skeleton generally shows the highest contrast on CT images. This approach determines the optimal segmentation threshold automatically, where the basic idea is to maximize the total information entropy of the object and background after segmentation. The procedure can be mathematically described as follows. Supposing a discrete random variable v stands for a threshold value by which the pixels on a CT image are divided into two groups, object and background, where the object is always brighter than the background in this case. Assuming the probability distributions of the object and background, D_O and D_B, are defined as Equation (1), the corresponding entropies, H_O and H_B, are expressed as Equation (2) respectively.

$$\begin{cases} D_O : \dfrac{P_0}{P_v}, \dfrac{P_1}{P_v}, \dfrac{P_2}{P_v}, ..., \dfrac{P_v}{P_v} \\ D_B : \dfrac{P_{v+1}}{1-P_v}, \dfrac{P_{v+2}}{1-P_v}, \dfrac{P_{v+3}}{1-P_v}, ..., \dfrac{P_{L-1}}{1-P_v} \end{cases} \tag{1}$$

$$\begin{cases} H_O(v) = \ln(1-P_v) + \dfrac{H-H_v}{1-P_v} \\ H_B(v) = \ln P_v + \dfrac{H_v}{P_v} \end{cases} \tag{2}$$

Where $P_v = \sum\limits_{i=0}^{v} P_i$, $H_v = -\sum\limits_{i=0}^{v} P_i \ln P_i$, $H = -\sum\limits_{i=0}^{L-1} P_i \ln P_i$ with P being the probability distribution, variables v and i being natural numbers, and constants V and L being positive integer. Hereby, the entropy of the whole CT image can be written as Equation (3), and the optimal threshold value shown as Equation (4) will be obtained when Equation (3) attains its maximum value.

$$H(v) = H_O(v) + H_B(v) = \ln P_v(1-P_v) + \dfrac{H_v}{P_v} + \dfrac{H-H_v}{1-P_v} \tag{3}$$

$$T_{optimal} = \arg \max_{v}(H(v)) \tag{4}$$

2.1.2. Body Outline and Lungs

Although the body outline and lungs do not exhibit higher contrast on CT images, they occupy a relatively larger area. Thus, a region growing method combined with thresholding is applied here to automatically segment these two structures. There usually exist some disadvantages when images are processed only by using an individual method. On the one hand, background noise whose greyscale value is close to the object will be inevitably left on the segmentation results using the single thresholding approach. On the other hand, it will result in over-segmentation or under-segmentation using the single region growing method when the object possesses an uneven gray level distribution or a fuzzy boundary. When integrating

thresholding and region growing, we could avoid the above problems by taking the following steps. Supposing $f(x,y)$ is the greyscale value function for an image, an optimal greyscale threshold T_1 can be achieved using the maximum class distance method, one of the classical thresholding algorithms. Afterwards, we therefore get Equation (5).

$$g(x, y) = \begin{cases} 1, & f(x, y) > T_1 \\ 0, & f(x, y) \leq T_1 \end{cases} \tag{5}$$

Furthermore, assuming R stands for the seed region, the mean greyscale value m and the standard deviation σ of the region R are respectively defined as:

$$\begin{cases} m = \dfrac{1}{n} \sum_{(k,l) \in R} f(k,l) \\ \sigma = \sqrt{\dfrac{1}{n} \sum_{(k,l) \in R} |f(k,l) - m|^2} \end{cases} \tag{6}$$

With $f(k,l)$ being the grayscale value function and n being the number of pixels in the seed region. The criterion for growth with a constraint condition is given in:

$$\begin{cases} |f(k,l) - m| \leq T_2 \\ f(k,l) \leq T_1 \end{cases} \tag{7}$$

Where $T_2 = \left(1 - \dfrac{\sigma}{m}\right) T_C$ with T_C being a control variable. The initial value of T_C can be estimated according to the initial seed region, and it will be adaptively adjusted during the region growing procedure until the target region is completely extracted.

2.1.3. Other Organs

Other major organs including heart and liver will be extracted by an atlas based automatic segmentation approach. The atlas used in this study was developed from ten sets of mice training data acquired by CT, whose anatomical structures have already been manually segmented. The following four steps are mainly involved in mathematically deriving this method. *To build an average-shape atlas*: Firstly, one volume data is selected from the ten sets of mice training data as the benchmark data. Then, the affine registration is performed using an algorithm presented by Slagmolend et al. [16]. Afterwords, a non-rigid registration based on a B-spline transformation model is utilized to process the datasets, where the registration measurement is determined by the weighted sum of the mutual information and surface distance. The non-rigid registration is conducted between every two datasets, so each dataset D_i will be processed nine times by Equation (8), finally generating 90 transformation fields $F_{ij(i \neq j)}$. The mean value of the transformation field for each dataset can be calculated by Equation (9), and subsequently we attain the average-shape atlas shown as Equation (10).

$$D_{i \rightarrow j} = F_{ij}(D_i) \tag{8}$$

$$\overline{F}_i = \frac{1}{9} \sum_{i \neq j} F_{ij} \tag{9}$$

$$D_{atlas} = \frac{1}{10} \sum_{i=1}^{10} \overline{F}_i(D_i) \tag{10}$$

To roughly localize the organs: This procedure can be generally regarded as the parameter (x,y,z) adjustment for the 3D translation of the registration, where x, y, z respectively stand for the offsets on the coronal, sagittal, and transversal planes. Prior to selecting an

appropriate value for z, a binary filter [17] is employed to roughly search the location of an organ from an experimental dataset. Then, assign the slice number of the coronal view with a maximum gray value for z. After finding the brightest slice from the average-shape atlas, move it to where z is, and (x,y) can be therefore adjusted by mapping the atlas to the experimental dataset. *To make precise registration*: A multi-resolution registration [18] is utilized to ensure the computational efficiency and robustness, whose basic idea is to add a pyramid filter [19] before making the registration between the fixed image and moving image. Furthermore, a B-spline transformation based on mutual information as a similarity measure is applied at last, which enables the deformation of an atlas organ to converge to the one of the experimental dataset.

2.1.4. Whole-body Integration

After obtaining the separated volumes of organs and tissues based on the above segmentation process, we need to fuse them into one volume data. During the automatic integration, priorities have been set for different organs and tissues to eliminate the inevitable overlaps and holes. Furthermore, to describe the behaviour of internal bioluminescent signals traveling inside living subjects, the corresponding optical properties for different parts have been assigned, which are measured by diffusion optical tomography. Finally, a heterogeneous mouse model has been completed.

2.2. Bioluminescence Tomography Reconstruction

For bioluminescence tomography, the diffusion equation and the Robin boundary condition are employed to model the light propagation in biological tissues [20], which are defined as:

$$\mu_a(\mathbf{x})\Psi(\mathbf{x}) - \nabla \cdot [D(\mathbf{x})\nabla\Psi(\mathbf{x})] = B(\mathbf{x}), \quad \mathbf{x} \in R \tag{11}$$

$$\Psi(\mathbf{x}) + 2f(r)D(\mathbf{x})[v(\mathbf{x}) \cdot \nabla\Psi(\mathbf{x})] = 0, \quad \mathbf{x} \in \partial R \tag{12}$$

Where D is the diffusion coefficient; μ_a is the absorption coefficient; $\mathbf{x}$ is the position vector; B is the bioluminescent source distribution; Ψ is the photon flux density; R is the region of biological tissues; f is the boundary mismatch factor between the biological tissues and air; r is the refractive index of the biological tissues; v is the unit outward normal on ∂R; and ∂R is the boundary of the biological tissues. In order to simplify the following computation instead of solving the above diffusion equation directly, the linear relationship between the measured outgoing photon density on the boundary and the unknown source distribution is built up in the matrix-vector form:

$$\mathbf{KB} = \mathbf{P} \tag{13}$$

Where $\mathbf{K}$ is the system matrix, standing for the optical properties of biological tissues; $\mathbf{P}$ is the measured outgoing photon density on the boundary.

The reconstruction procedure in bioluminescence tomography aims to recover the signal source distribution B in Equation (13). However, it is an underdetermined system of linear equations with fewer equations than unknowns, which is known as an ill-posed problem. A popular method [21] to reduce the ill-posedness is to introduce anatomical structure information as *a priori* knowledge. The simplest solution to Equation (13) is expressed as Equation (14), where the least square approach has been applied [22], but it usually magnifies noise error. To further enhance the practicability, the Tikhonov regularization method has been commonly utilized for an alternative [23]. The object function with the l_2 norm constraint is given as Equation (15), where λ is the regularization parameter and $\|\cdot\|_2^2$ stands for the l_2 norm. Therefore, the internal source distribution can be finally solved by applying optimal minimization to the object function.

$$\arg\min_{B}\left[\frac{1}{2}\|\mathbf{KB} - \mathbf{P}\|_2^2\right] \tag{14}$$

$$\arg\min_{B}\left[\frac{1}{2}\|\mathbf{KB}-\mathbf{P}\|_2^2 + \lambda\|\mathbf{B}\|_2^2\right] \qquad (15)$$

3. Results and Discussion

The acquired CT projection data was originally in DICOM format, which was then converted into 3D volume data by the FDK algorithm [24]. Afterwards, the volume data with a size of 512×512×512 was automatically segmented, where the total accumulated segmentation time is less than 10 minutes. The results are displayed in the following pictures, among which the separated volumes of organs and tissues are described in Figure 1 to 4 while the ultimate whole-body integration is visualized in Figure 5.

The result in Figure 1a suggests that the thresholding method based on the principle of maximum entropy can be utilized to provide a precise segmentation of bone structures. It took less than 5 seconds to complete the automatic procedure. As shown in Figure 1b, the surface of the experimental mouse body is rendered based on its segmented body outline.
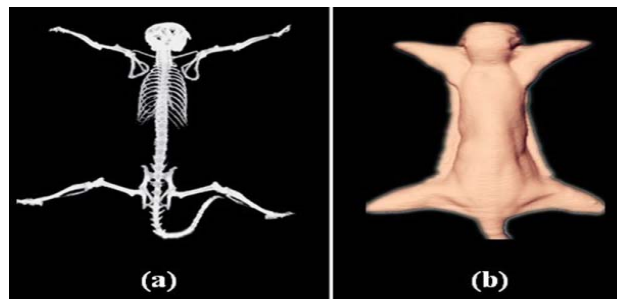
Figure 1. The Results of Bone and Body Segmentation: (a) the segmented bone structures, (b) the segmented body outline.
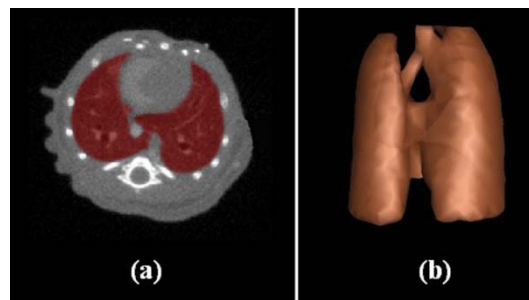
Figure 2. The Results of Lung Segmentation: (a) a CT slice in transversal view with a marked region in the lungs, (b) the segmented lungs rendered in 3D.
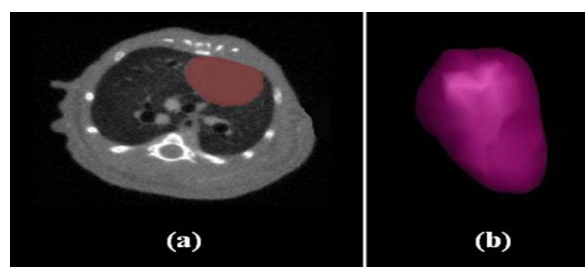
Figure 3. The Results of Heart Segmentation: (a) a CT slice in transversal view with a marked region in the heart, (b) the segmented heart rendered in 3D.

The segmentation results of the mouse organs are given in Figure 2 to 4. The lungs are processed by a region growing method combined with thresholding, which is relatively easy to realize. The results shown in Figure 2 suggest that this approach guarantees good region consistence. Since the other soft tissues such as the heart and liver are in the lower gray-value contrast, an atlas based automatic segmentation approach is applied to obtain the results exhibited in Figure 3 and Figure 4.
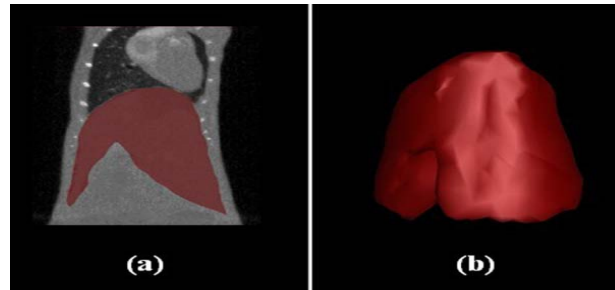
Figure 4. The Results of Liver Segmentation: (a) a CT slice in coronal view with a marked region in theliver, (b) the segmented liver rendered in 3D.
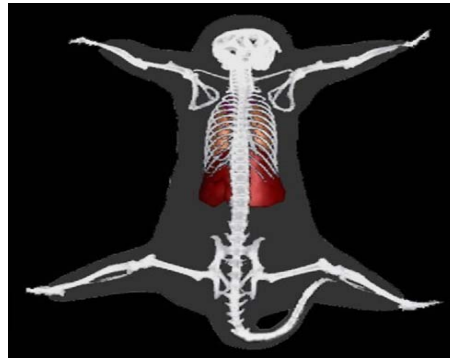
Figure 5. The Heterogeneous Mouse Model after whole-body Integration.

Figure 6 shows the two reconstruction results for bioluminescence tomography. In the first case, a homogeneous mouse model without any anatomical information is utilized to recover the internal bioluminescent source signal, and the corresponding results can be seen in Figure 6a. In the second case, the anatomical structure is taken as *a priori* knowledge for the reconstruction, which obviously leads to more accurate reconstruction results shown in Figure 6b.
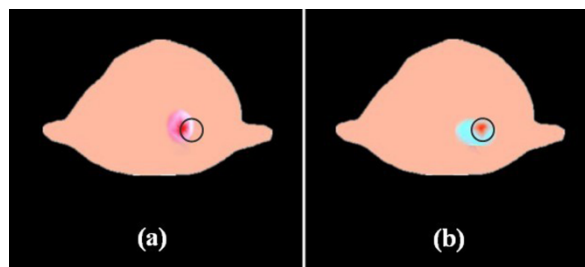
Figure 6. The Reconstruction Results of Bioluminescence Tomography in Cross-sectional Views: (a) the reconstruction results based on a homogeneous mouse model, (b) the reconstruction results based on a heterogeneous mouse model, where the circle represents the real location of the bioluminescent source.

4. Conclusion

To validate the feasibility of this method, the raw datasets of the two imaging modalities have been achieved via an *in vivo* mouse experiment. Subsequently processed by the proposed segmentation method, the anatomical mouse model has been automatically built up, which can guarantee computational efficiency. Further validated by the reconstruction comparison, this heterogeneous model is capable of ensuring the accuracy of bioluminescence tomography.

References

[1] Prescher JA, Contag CH. Guided by the light: visualizing biomolecular processes in living animals with bioluminescence. *Current Opinion in Chemical Biology.* 2010; 14(1): 80-89.

[2] Leppanen O, Ekstrand M, Braesen JH. Bioluminescence imaging of energy depletion in vascular pathology: patent ductus arteriosus and atherosclerosis. *Journal of Biophotonics.* 2012; 5(4): 336-344.

[3] Hashizume R, Ozawa T, Dinca EB. A human brainstem glioma xenograft model enabled for bioluminescence imaging. *Journal of Neuro-Oncology.* 2010; 96(2): 151-159.

[4] Hu H, Liu J, Yao L. Real-time bioluminescence and tomographic imaging of gastric cancer in a novel orthotopic mouse model. *Oncology Reports.* 2012; 27(6): 1937-1943.

[5] Shavkunov A, Panova N, Prasai A. Bioluminescence methodology for the detection of protein-protein interactions within the voltage-gated sodium channel macromolecular complex. *Assay and Drug Development Technologies.* 2012; 10(2): 148-160.

[6] Turner D, Sun J, Nelson S. Quantitative analysis of bacteriophage plaque expansion by bioluminescence imaging. *Luminescence.* 2012; 27(2): 167-169.

[7] Cong W, Wang G. *Iterative method for bioluminescence tomography based on the radiative transport equation.* Proceedings of the Society of Photo-optical Instrumentation Engineers, San Diego. 2006; 6318: 31826-31826.

[8] Cong W, Wang G. Boundary integral method for bioluminescence tomography. *Journal of Biomedical Optics.* 2006; 1: 020503-1-020503-3.

[9] Klose AD. Ntziachristos V, Hielscher AH, The inverse source problem based on the radiative transfer equation in optical molecular imaging. *Journal of Computational Physics.* 2005; 202: 323-345.

[10] Slavine NV, Lewis MA. Richer E, Antich PP. Iterative reconstruction method for light emitting sources based on the diffusion equation. *Medical Physics.* 2006; 33: 61-68.

[11] Smeets D, Loeckx D, Stijnen B. Semi-automatic level set segmentation of liver tumors combining a spiral-scanning technique with supervised fuzzy pixel classification. *Medical Image Analysis.* 2009; 14(1): 13-20.

[12] Piccini D, Littmann A, Nielles-Vallespin S. Respiratory self-navigation for whole-heart bright-blood coronary MRI: Methods for robust isolation and automatic segmentation of the blood pool. *Magnetic Resonance in Medicine.* 2012; 68(2): 571-579.

[13] Bai J, Trinh TH, Chuang KH. Atlas-based automatic mouse brain image segmentation revisited: model complexity vs. image registration. *Magnetic Resonance Imaging.* 2012; 30(6): 789-798.

[14] Lai J, Xie M. Segmentation lung fields in thoracic CT scans using manifold method. *Telkomnika.* 2012; 10(5): 1005-1014.

[15] Sun J. A new image segmentation algorithm and its application in lettuce object segmentation. *Telkomnika.* 2012; 10(3): 557-563.

[16] Slagmolen P, Elen A, Seghers D, Loeckx D, Maes F, Haustermans K. *Atlas based liver segmentation using nonrigid registration with a B-spline transformation model,* Proceedings of International Conference on Medical Image Computing and Computer Assisted Intervention. Brisbane. 2007; 197-206.

[17] Martinez-Corral M, Andres P, Zapata-Rodriguez CJ. Three-dimensional superresolution by annular binary filters. *Optics Communications.* 1999; 165(4-6): 267-278.

[18] Alhichri HS, Kamel M. Multi-resolution image registration using multi-class Hausdorff fraction. *Pattern recognition letters.* 2002; 23(1-3): 279-286.

[19] Aiazzi B, Alparone L, Baronti S. Pyramid-based multiresolution adaptive filters for additive and multiplicative image noise. *IEEE Transactions on Circuits and Systems II: Analog and Digital Signal Processing.* 1998; 45(8): 1092-1097.

[20] Arridgey SR, Hebdenz JC. Optical imaging in medicine II: modelling and reconstruction. *Physics in Medicine and Biology.* 1997; 42: 841-853.

[21] Zacharopoulos AD, Svenmarker P, Axelsson J, Schweiger M, Arridge SR. Andersson-Engels S, A matrix-free algorithm for multiple wavelength fluorescence tomography. *Optics Express.* 2009; 17: 3025-3035.

[22] Paige CC, Saunders MA. LSQR – an algorithm for sparse linear-equations and sparse least-squares. *ACM Transactions on Mathematical Software.* 1982; 8(1): 43-71.

[23] Calamante F, Gadian DG, Connelly A. Quantification of bolus-tracking MRI: Improved characterization of the tissue residue function using Tikhonov regularization. *Magnetic Resonance in Medicine*. 2003; 50(6): 1237-1247.

[24] Pan X, Sidky EY, Vannier M. Why do commercial CT scanners still employ traditional, filtered back-projection for image reconstruction? *Inverse Problems*. 2009; 25(12): 123009.